

Oriented Thiophene-Extended Benzotrithiophene Covalent Organic Framework Thin Films: Directional Electrical Conductivity

Laura Frey, Jonas Fredrik Pöhls, Matthias Hennemann, Andre Mähringer, Stephan Reuter, Timothy Clark,* Ralf Thomas Weitz,* and Dana Dina Medina*

The synthesis of covalent organic frameworks (COFs) based on a novel thiophene-extended benzotrithiophene (BTT) building block is described, which in combination with triazine-based amines (1,3,5-triazine-2,4,6-triyl) trianiline (TTA) or (1,3,5-triazine-2,4,6-triyl)tris((1,1'-biphenyl)-4-amine) (TTTBA) affords crystalline, and porous imine-linked COFs, BTT TTA and BTT TTTBA, with surface areas as high as 932 and 1200 m² g⁻¹, respectively. Oriented thin films are grown successfully on different substrates, as indicated by grazing incidence diffraction (GID). Room-temperature in-plane electrical conductivity of up to 10⁻⁴ S m⁻¹ is measured for both COFs. Temperature-dependent electrical conductivity measurements indicate activation energies of ≈123.3 meV for BTT TTA and ≈137.5 meV for BTT TTTBA and trap-dominated charge transport via a hopping mechanism for both COFs. Moreover, conductive atomic force microscopy reveals directional and defect-dominated charge transport in the oriented BTT COF films with a strong preference for the in-plane direction within the molecular 2D-planes. Quantum mechanical calculations predict BTT TTTBA to conduct holes and electrons effectively in both in-plane and out-of-plane directions. In-plane, charge carrier transport is of hopping character where the triazine cores represent the barrier. Out-of-plane, a continuous charge-carrier pathway is calculated that is hampered by an imposed structural defect simulated by a rotated molecular COF layer.

blocks. The slightly reversible nature of the covalent bond-formation ensures “proof-reading” related to building block assembly faults, leading to the formation of highly structurally defined products.^[1] The use of organic building blocks has opened up the opportunity to construct tailor-made COFs, whose key properties such as pore structure, optical properties, and conjugation of monomers can be modified by fine-tuning of the chemical structure and geometry of the building blocks. These unique features of COFs provide access to study chemical character – structural paradigm – performance correlations for a variety of applications such as gas storage,^[2] sensing,^[3] catalysis,^[4] and separation.^[5] Inspired by photoactive and semiconducting organic polymers, COFs consisting of photoactive building blocks have been synthesized. Typically, the building blocks feature geometries suitable for constructing 2D COF sheets, extended in-plane, upon polymerization. The nascent molecular COF sheets grow in size and interact, aggregate and fall out

of solution as a layered solid. The 2D-COF structure paradigm provides several intriguing structural properties, such as precise positioning of the organic moieties in a columnar manner, in-plane conjugation, accessible pore channels, and a large variety of pore sizes and shapes. In 2D electroactive conjugated COFs,

1. Introduction

Covalent organic Frameworks (COFs) are crystalline, highly ordered, porous polymers that are formed mainly by reversible condensation reactions of a large selection of organic building

L. Frey, A. Mähringer, S. Reuter, D. D. Medina
Department of Chemistry and Center for Nanoscience (CeNS)
Ludwig-Maximilians University (LMU)
Butenandtstraße 11 (E), 81377 Munich, Germany
E-mail: dana.medina@cup.uni-muenchen.de

 The ORCID identification number(s) for the author(s) of this article can be found under <https://doi.org/10.1002/adfm.202205949>.

© 2022 The Authors. Advanced Functional Materials published by Wiley-VCH GmbH. This is an open access article under the terms of the Creative Commons Attribution-NonCommercial-NoDerivs License, which permits use and distribution in any medium, provided the original work is properly cited, the use is non-commercial and no modifications or adaptations are made.

DOI: 10.1002/adfm.202205949

J. F. Pöhls, R. T. Weitz
Institute of Physics
Faculty of Physics
Georg-August-University Göttingen
37077 Göttingen, Germany
E-mail: thomas.weitz@uni-goettingen.de

M. Hennemann, T. Clark
Computer-Chemistry-Center
Department of Chemistry & Pharmacy
Friedrich-Alexander-University Erlangen-Nürnberg (FAU)
Naegelsbachstraße 25, 91052 Erlangen, Germany
E-mail: tim.clark@fau.de

R. T. Weitz
International Center for Advanced Studies of Energy Conversion (ICASEC)
University of Göttingen
37073 Göttingen, Germany

charge migration is expected both in the plane of the conjugated COF sheets and perpendicular thereto via the columns. The study of charge migration in 2D-COFs benefits from deposition with a preferential layer orientation with respect to the surface, which in turn allows charge migration to be probed, both in the conjugated plane and in the noncovalent molecular columns of the COF.^[6] In recent years, research on multi(thiophene)-fused aromatic compounds has gained interest owing to their successful implementation as active materials in organic light-emitting diodes,^[7] photovoltaic devices,^[8,9] or organic thin-film transistors (OTFTs).^[10] Moreover, much effort has been devoted to the synthesis on benzo[1,2-*b*:4,5-*b'*]dithiophene (BDT) and benzo[1,2-*b*:3,4-*b'*:5,6-*b''*]trithiophene (BTT) derivatives as potential organic semiconductors.^[11] Benzotrithiophene comprises three thiophenes fused to a central benzene ring, resulting in a planar and electron-rich system.^[12,13] The BTT core and its different isomers have been used successfully as part of a polymeric active layer in organic solar cells,^[9,14] aggregation agent promoting self-assemblies^[15] and 2D-covalent organic frameworks.^[16] Extended BTT, and particularly thiophene-extended BTT cores suitable for the formation of COFs has not yet been reported. In the context of COFs, designing an extended BTT photoactive core requires solubility and symmetry to be considered for COF formation. This includes extension of the BTT core in three vertices with the desired functional groups and the installation of solubilizing side chains that synchronize and are compatible with the COF layer stacking.^[17]

We now describe the synthesis of a novel three-pod thiophene extended benzotrithiophene (BTT)-based tricarbaldehyde that features the central BTT-unit decorated with three peripheral thiophene moieties. Combining the novel BTT building block with multidentate amines, namely (1,3,5-triazine-2,4,6-triyl)trianiline (TTA) or (1,3,5-triazine-2,4,6-triyl)tris((1,1'-biphenyl)-4-amine) (TTTBA), two novel, highly crystalline and porous imine-linked COFs, termed BTT TTA and BTT TTTBA, respectively, are presented. The presence of the peripheral thiophene units at the BTT core building block leads to the formation of squished hexagonal pores. Moreover, highly oriented, crystalline thin films were successfully grown on different substrates, featuring layer orientation parallel to the substrate and thickness of 300–500 nm. BTT TTA and TTTBA films show light absorption in the 300–600 nm wavelength range and photoluminescence (PL) emission at 740 nm and 705 nm for BTT TTA and TTTBA, respectively. Directional electrical conductivity of the BTT COF films was determined by constructing various devices of different electrode architectures. Room temperature in-plane electrical conductivity values as high as 10^{-4} S m^{-1} was determined for BTT TTA and TTTBA. Temperature-dependent electrical conductivity measurements indicate trap-dominated charge transport in-plane.

2. Results and Discussion

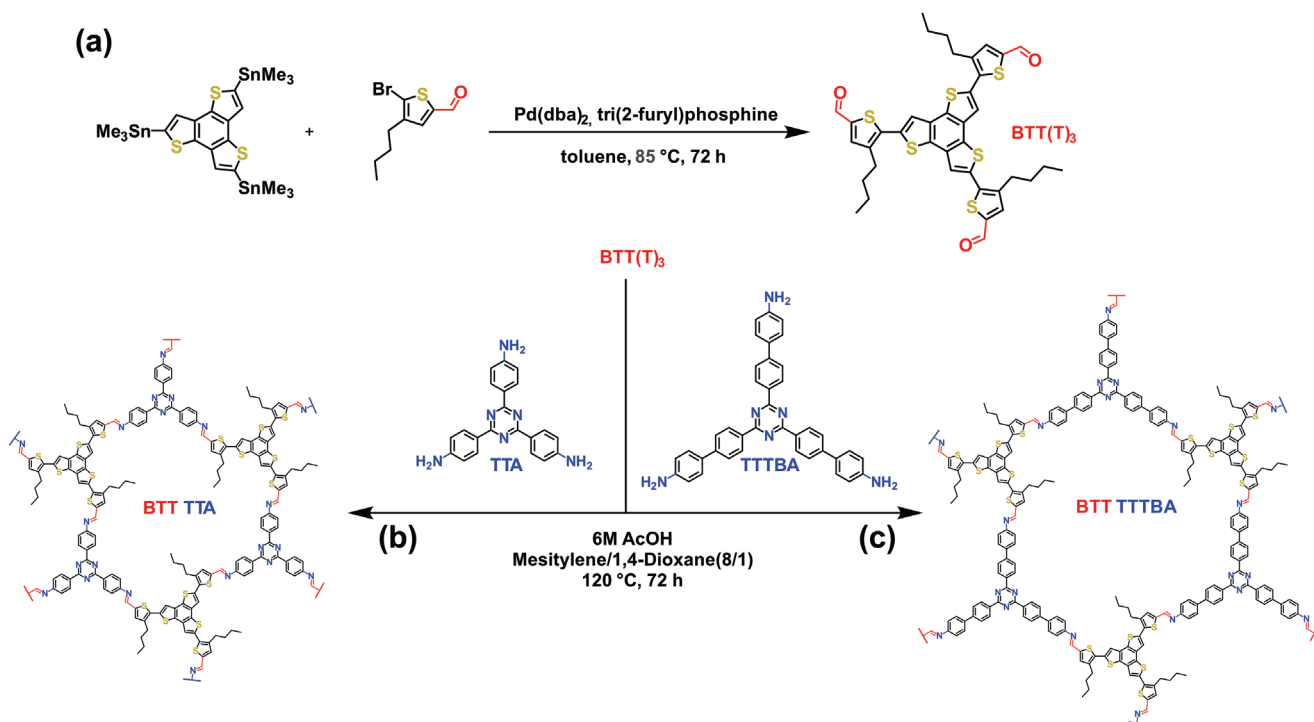
2.1. Synthesis

We aimed at synthesizing COF building blocks containing six conjugated thiophene units. Therefore, initially, the novel

terthieno-benzotrithiophene (BTT)-based COF building block, termed BTT(T)₃, was synthesized. First, the BTT core was obtained following a reported protocol.^[13] Subsequently, the BTT core was stannylated and coupled to 5-bromo-4-butylthiophene-2-carbaldehyde through a *Stille* coupling reaction (Scheme 1) to afford the desired building block, BTT(T)₃ (for more information see Supporting Information). The as-prepared BTT(T)₃ building block was suspended in mesitylene and 1,4-dioxane (8:1, v:v) together with (1,3,5-triazine-2,4,6-triyl)trianiline (TTA) or (1,3,5-triazine-2,4,6-triyl)tris((1,1'-biphenyl)-4-amine) (TTTBA) as complementary building blocks. Employing a Schiff-base acid-catalyzed imine condensation reaction under solvothermal synthesis conditions for 72 h at 120 °C resulted in the precipitation of a dark orange powder for BTT TTA and dark yellow powder for TTTBA (Scheme 1). After the given reaction time, the precipitated powders were filtered under reduced pressure and washed with THF. The wet powders were subjected to supercritical CO₂ extraction for further drying^[18] (for further information see Figure S1 and Section B, Supporting Information).

In models, the presence of the peripheral thiophene units at the BTT core results in a rigid and chiral building block, subsequently leading to the formation of highly distorted hexagonal pores (Figure S2, Supporting Information). These two features typically limit the formation of a crystalline product.^[19] The formation of highly crystalline BTT TTA and TTTBA materials was confirmed using powder X-ray diffraction (PXRD) analysis (Figure 1c,f). Impressively, the obtained BTT COFs feature long-range order with observed high order Bragg reflections in the case of BTT TTA. The PXRD diffraction patterns reveal highly defined and intense reflections at 3.8°, 6.6°, 10.1°, 13.1°, 15.2°, 16.6°, and 25.7° 2θ for BTT TTA and 2.9°, 5.1°, 5.9°, and 7.9° 2θ for BTT TTTBA. According to the symmetry of the building blocks, structure models were constructed using the Materials Studio software package (Accelrys Inc.), the structure simulations and geometry optimization were carried out using the Forcite module employing the universal force field and *P1* symmetry. The resulting theoretical PXRD patterns were compared to those obtained experimentally. In 2D-COFs, different stacking arrangements of the 2D layers are possible; eclipsed layer stacking (AA), alternating, staggered, or unidirectional stacking as well as a random arrangement.^[20] For both COFs, the simulations show that the eclipsed layer stacking (AA) and unidirectional stacking agree well with the experimental patterns. For both models, unit-cell parameters suggest structures close to a hexagonal crystal system; however, considering the packing of the alkyl side chains, we ruled out a fully overlapped AA stacking of the layers, hence for further refinement of the unit cell we used unidirectional stacking model (Figure 1a–c,f).

The simulated unit cells obtained were refined using the Reflex module in the Materials Studio software using the Pawley method for powder refinement according to the experimentally obtained PXRD patterns. Thereby, unit cell parameters of $a = 277$ Å, $b = 28.0$ Å, $c = 3.7$ Å, $\alpha = \beta = 90^\circ$, $\gamma = 122^\circ$ for BTT TTA and $a = 34.4$ Å, $b = 35.1$ Å, $c = 4.0$ Å, $\alpha = 89^\circ$, $\beta = 90^\circ$, $\gamma = 120^\circ$ for BTT TTTBA were obtained. Additionally, the observed reflections at the PXRD patterns were indexed and attributed to the corresponding *hkl* planes. For BTT TTA,



Scheme 1. a) A Stille coupling reaction scheme, affording the tricarbaldehyde BTT(T)₃ building block. Schematic representation of the synthesis of b) BTT TTA, using 4,4',4''-(1,3,5-triazine-2,4,6-triyl)trianiline (TTA) and c) BTT TTTBA using 4,4''',4''''-(1,3,5-triazine-2,4,6-triyl)tris((1,1'-biphenyl)-4-amine) (TTTBA) as complementary building blocks.

hkl (100), (110), (210), (220), (400), (230), and (001) correspond to 3.8°, 6.6°, 10.1°, 13.1°, 15.2°, 16.6°, and 25.7° 2 θ . For BTT TTTBA, *hkl* (100), (110), (200), and (210) correspond to 2.9°, 5.1°, 5.9°, and 7.9° 2 θ . For BTT TTA COF, a reflection associated with the stacking distance at 25.7° 2 θ was obtained, corresponding to an interlayer distance of \approx 3.5 Å.

The porosity of the two BTT COFs was analyzed by nitrogen gas physisorption at 77 K. For BTT TTA, the nitrogen sorption isotherm shows typical type I sorption profile with a sharp nitrogen uptake at relatively low partial pressure ($p/p_0 < 0.09$ and up to 240 cm³ g⁻¹), which is characteristic for microporous materials. The nitrogen sorption isotherm of BTT TTTBA features type IVb sorption isotherm profile.^[21] In the isotherm, two steep and well-defined nitrogen uptakes at low partial pressures ($p/p_0 < 0.17$ and up to 320 cm³ g⁻¹) related to the presence of a mesoporous material are shown. In addition, the adsorption isotherm is fully reversible, showing no hysteresis, which is a common feature of materials containing aligned 1D-mesopores with diameter smaller than 40 Å.^[22] Both BTT TTA and BTT TTTBA revealed high porosity with apparent and calculated Brunauer–Emmett–Teller (BET) surface areas of 932 and 1200 m² g⁻¹, respectively (Figure 1d,g; Figure S4, Supporting Information). For the analysis of the pore sizes, the quenched solid density functional theory (QSDFT) model was employed. Thereby, pore sizes of 1.8 and 2.6 nm with a narrow pore size distribution were determined for BTT TTA and BTT TTTBA, respectively (Figures S5 and S6, Supporting Information).

Thermogravimetric analysis (TGA) under synthetic air flow revealed that both BTT COFs are thermally stable at temperatures up to 350 °C. Here, significant weight loss at \approx 350 °C

associated with the beginning of a structural degradation of the COF materials is detected; at 600 °C the process ceases with complete weight loss (Figure S7, Supporting Information). Notably, the continuous and complete weight loss is an excellent indication for the high purity of the COF materials and the absence of residual synthesis agents originating from ligand synthesis. Scanning electron microscopy (SEM) analysis of the COF powders revealed nanometer-sized COF particles of \approx 50–150 nm in diameter which aggregate into cauliflower-like assemblies of different sizes (Figure S8, Supporting Information). We note that the majority of the COF crystallites appear spherical. However, in some cases faceted, hexagonally shaped crystallites are clearly observed, which corresponds well with the high structural definition observed by PXRD and the simulated pseudo-hexagonal structure. Transmission electron microscopy (TEM) analysis of both COFs further supports the highly crystalline nature of the COFs. Projections along the *c*-axis reveal the expected honeycomb structure of the COF (Figure 1e,h). Electron diffraction patterns of the obtained images further support the formation of highly crystalline COFs, showing high order diffraction lines for a single BTT TTTBA crystallite (Figure S9, Supporting Information).

2.2. Oriented Thin Films of BTT TTA and BTT TTTBA

To study and characterize the BTT COF properties regarding their photophysical and electronic properties further, oriented COF thin films were synthesized on various substrates. The synthesis was carried out in glass vessels equipped

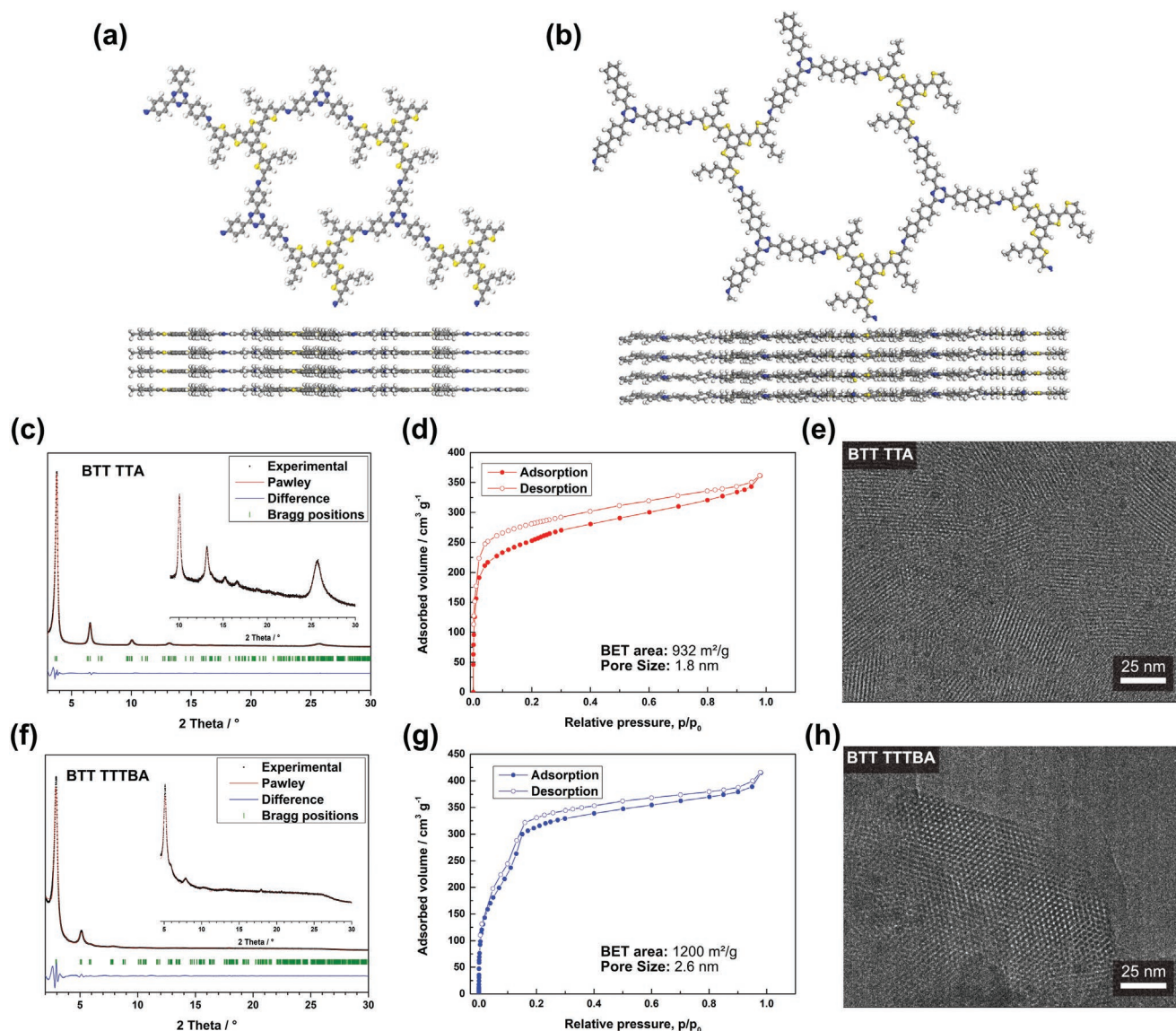


Figure 1. a,b) Schematic representation of BTT TTA and BTT TTTBA. c,f) Experimental PXRD pattern (black dots) of BTT TTA and TTTBA COF, respectively. Pawley refinement (red line), difference plot between the experimental data and the Pawley-refined PXRD pattern (blue line), Bragg reflection positions are indicated by green ticks. The insets in both XRD patterns show a magnified view of $2\theta > 5^\circ$. d,g) Nitrogen physisorption isotherms at 77 K of BTT TTA and BTT TTTBA, respectively. e,h) TEM images of BTT TTA and BTT TTTBA bulk material, respectively.

with a Teflon substrate holder using the non-epitaxy in situ approach under developed solvothermal synthesis protocols for the BTT COFs.^[6,23] Thus, the substrates were positioned and immersed horizontally using a Teflon substrate holder into the reaction vessel, charged with the appropriate reactive precursor solution. Subsequently, acetic acid was added, and the reaction vessel was heated to 120 °C for a fixed reaction time (ranging from 12 to 72 h, depending on the desired thickness of the film). After removal from the reaction mixture, the substrate was thoroughly washed with dry tetrahydrofuran (THF) and dried under a stream of nitrogen to reveal a homogeneous shimmering layer on the substrate. SEM cross section and top-view images showed that a continuous and homogeneous coverage of the substrate was

obtained (Figure 2d,e; Figures S10 and S11, Supporting Information). Depending on the reaction time, the thickness of the resulting COF layer is tuned, ranging from 320 to 590 nm for BTT TTA and 290 to 480 nm for BTT TTTBA (Figure S12, Supporting Information).

A coplanar grazing incidence X-ray diffraction (GIXRD) analysis indicated the preferential parallel orientation of the COF molecular layers with respect to the substrate, with the (001) reflection (at 25.7° and 26.2° 2θ for BTT TTA and BTT TTTBA, respectively) being the only reflection visible in the diffraction pattern (Figure S13, Supporting Information). Complementary to the 1D-diffractogram, grazing-incidence small and wide-angle X-ray scattering analysis (GI-SWAXS) was carried out to examine the crystallinity of the films and

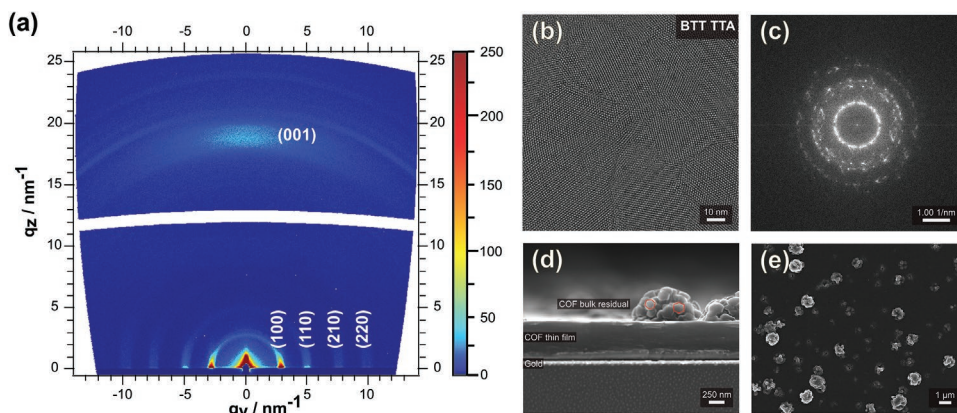


Figure 2. a) GIWAXS 2D patterns of BTT TTA thin film grown on ITO. b,c) TEM and electron diffraction images of BTT TTA thin films on ITO scratched off the substrate. d,e) SEM cross section and top-view images of BTT TTA thin films on gold-coated glass substrates.

to confirm the preferential orientation of the COF crystallites with respect to the substrate. For both COFs, strong distinct reflections at q_y 2.78, 4.89, 7.56, 9.82 nm^{-1} and q_z 19.13 nm^{-1} for BTT TTA corresponding to hkl (100), (110), (210), (220), (001) and q_y 2.18, 3.86, and 5.85 nm^{-1} for BTT TTTBA corresponding to hkl (100), (110), and (210) were obtained. The q -values obtained by data-reduction to 1D-plots match those obtained for the bulk powder XRD patterns (Figure S14, Supporting Information). The GIWAXS data of both COF thin films confirm the preferential orientation with the [001]-axis (c -axis) to be oriented orthogonal to the surface (Figure 2a; Figure S11a, Supporting Information). The SEM cross section and top-view images showed that in both cases a homogeneous and continuous COF deposit was obtained with residual powder that is attributed to a secondary nucleation on top of the oriented thin films. High-magnification SEM micrographs targeting the crystallites on top of the film revealed hexagonal facets, which is in line with the observed bulk COF morphology (Figure 2d,e; Figure S11, Supporting Information). Additionally, TEM analysis of scratched-off film confirms the formation of highly oriented COF crystallites that form a continuous tile; (Figure 2b,c; Figure S11, Supporting Information) projections along the c -axis reveal the expected honeycomb structure of the COF. Furthermore, electron diffraction of the non-oriented residual deposit on top of the oriented film reveals highly crystalline COF materials.

2.3. Photophysical Properties

Next, we analyzed the photophysical properties of the BTT COFs using UV-vis and photoluminescence (PL) spectroscopies (Figure 3). For both BTT COF samples examined, the absorption bands are located in the UV and blue spectral regions. Further, the BTT TTA has an absorption onset of ≈ 560 nm. The absorption spectrum of BTT TTTBA is slightly blueshifted compared to the BTT TTA. We attribute this effect to the additional benzene rings in TTTBA being rotated out-of-plane, which can affect the extent of conjugation (Figure 3a). This shift can also be seen in the color of the resulting thin films, with BTT TTA films revealing bright orange and BTT TTTBA films bright yellow colors. Assuming a direct bandgap transition, Tauc plots allowed for estimating the optical band gaps of the two structures, yielding band gaps of 2.32 eV for BTT TTA and 2.41 eV for BTT TTTBA (Figure 3b). Steady-state PL of the BTT COFs was measured at an excitation wavelength of 378 nm. BTT TTA exhibits two distinct emission bands at ≈ 575 and 740 nm, the latter being more intense. For BTT TTTBA, only one distinct emission band was detected at ≈ 705 nm. Both COFs show broad emissions that range from the green to the near-infrared spectral regions (Figure 3c). When compared to the PL emissions of the BTT(T)₃ building block a significant red-shift of the emission bands of the corresponding COFs can be

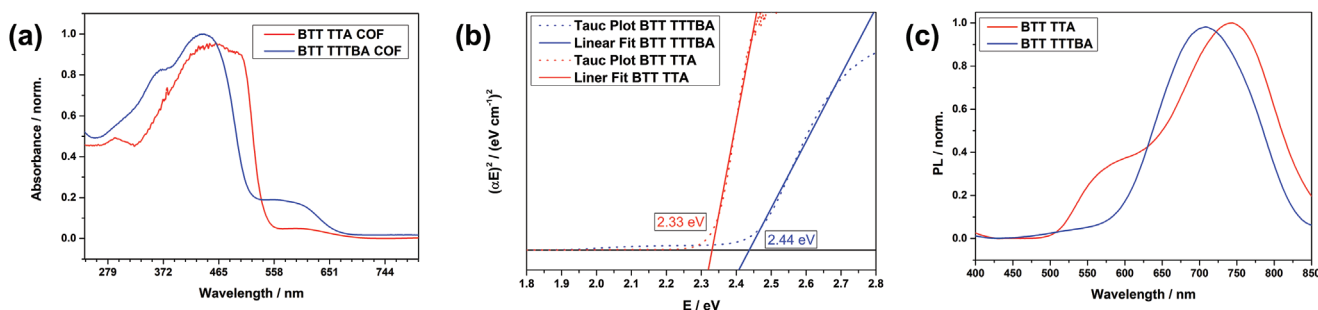


Figure 3. a) Normalized absorption spectra of BTT TTA (red) and BTT TTTBA COF (blue) thin film on quartz substrates. b) Tauc plots of the BTT TTA (red) and BTT TTTBA (blue) UV-vis absorbance spectra calculated for a direct band transition model. c) Normalized PL ($\lambda_{\text{exc}} = 378$ nm) spectra for BTT TTA (red) and BTT TTTBA (blue) thin films.

detected, indicating the formation of a new electronic structure with extended conjugation on framework COF formation (Figure S15, Supporting Information).

2.4. Electrical Conductivity in Oriented Thin Films of BTT TTA and BTT TTTBA COFs

Electrical conductivity measurements were used to assess the charge-transport properties of the BTT COFs, both in-plane along the 2D molecular sheets and out-of-plane across the stacked 2D-COF columns. The temperature-dependent electrical conductivity was determined using two-probe measurements in the temperature range from 296 to 6 K. The measurements were performed on macroscopic COF films (thickness ≈ 500 nm) that had been deposited onto silicon wafers coated with an insulating layer of 300 nm SiO_2 . The voltage sweeps performed for the BTT TTA, exemplarily shown for different temperatures in Figure 4b, are nonlinear, which we attribute to the impact of non-ideal injection at the COF-gold contact.^[24] The temperature-dependent conductivity values presented in Figure 4a are therefore determined at drain-source voltage (V_{DS}) = 40 V, since the influence of the contact resistance is less pronounced at such high voltages.^[25] At room temperature, this results in a conductivity of $\approx 8.7 \times 10^{-4} \text{ S m}^{-1}$ for of BTT TTA and $\approx 1.1 \times 10^{-4} \text{ S m}^{-1}$ for BTT TTTBA, which places them among the most conductive non-doped COFs reported to date.^[26] Notably, in-plane conductivity measurements of films of different thicknesses (320, 380, and 590 nm in the case of BTT TTA and 290, 430, and 480 nm in the case of BTT TTTBA) show similar conductivity values.

The temperature-dependent data in Figure 4a reveal thermally activated in-plane conductivity for both COFs. Activation energies (E_a) can be derived from fitting an Arrhenius plot of the form $\sigma(T) = \sigma_0 \exp[-(E_a/k_B T)]$ (with the Boltzmann constant k_B) to the conductivity data σ plotted against the inverse of the temperature T^{-1} . The activation energies E_a derived by this method are ≈ 123.3 meV for BTT TTA and ≈ 137.5 meV for BTT TTTBA. Based on the electrical conductivity data obtained, it is challenging to determine whether the activated behavior arises due to a band gap in the electronic structure or by charge traps in the form of defects. In the case of semiconductors with doping levels below the electrostatically accessible range ($\approx 10^{12} \text{ cm}^{-2}$ in our geometry), electrical conductivity can be altered by varying the charge-carrier density using a gate voltage. In the case of BTT COFs, such an effect was not observed. This, together with the band gaps obtained from the Tauc plots (Figure 3b), which are an order of magnitude larger than the activation energies determined, suggests that the activated behavior observed is rather defect related. Such defects might be present at boundaries between single-crystalline grains. Furthermore, the low-temperature conductivity data are in good agreement with the characteristic temperature dependence of Mott variable-range hopping, which could indicate hopping-based transport.

In contrast to the conductivities, up to $8.7 \times 10^{-4} \text{ S m}^{-1}$ reached for the in-plane measurements, charge transport in the out-of-plane direction is strongly suppressed. Two-point measurements on a macroscopic scale with an indium tin oxide (ITO) bottom contact and a gold top contact show a room-temperature conductivity of $\approx 9.5 \times 10^{-11} \text{ S m}^{-1}$ with a strong temperature dependence for the BTT TTTBA (Figure 4e).

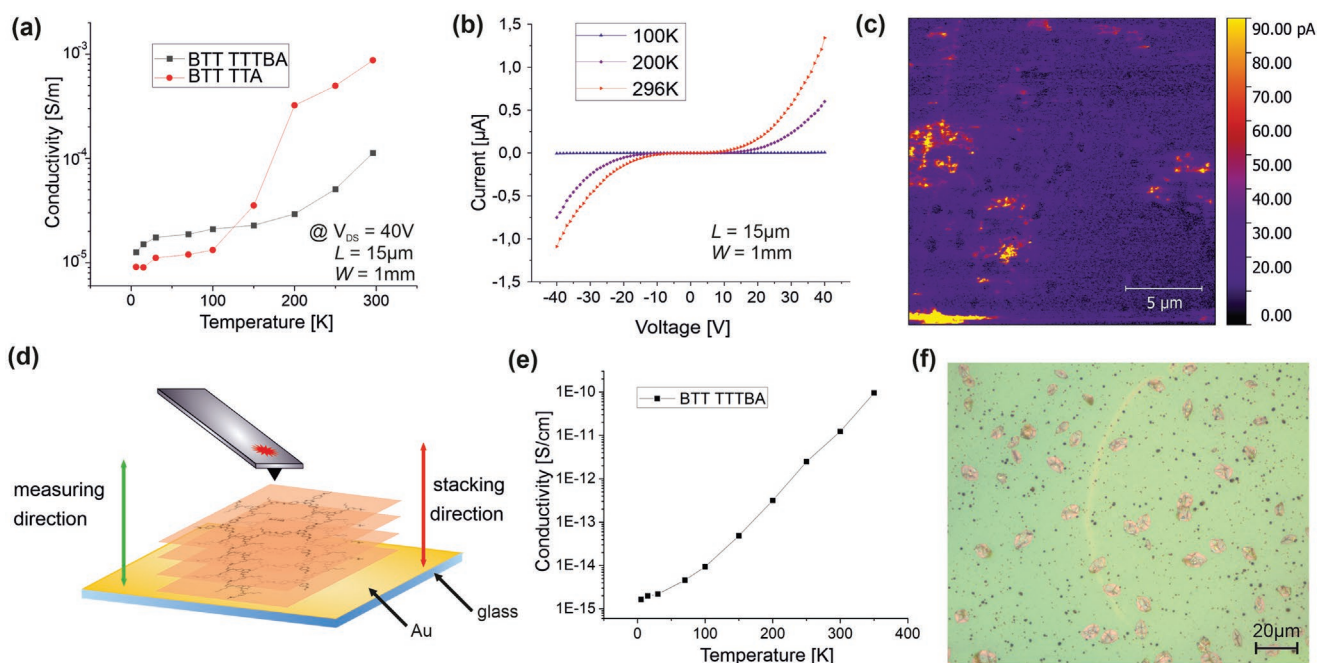


Figure 4. a) Temperature dependent electrical conductivity measurements of BTT TTA and BTT TTTBA in the in-plane direction. Conductivities calculated from two-point measurements in the temperature range from 6 to 296 K. b) The underlying I - V curves, shown for 100 K, 200 K, and room temperature for BTT TTA reveal a significant impact of contact resistance. c) cAFM measurement on the BTT TTTBA film on Au. d) Schematic representation of the out-of-plane conductive AFM measurements of the thin BTT COF films. e) Temperature dependence of the out-of-plane conductivity for the BTT TTTBA. f) The polycrystalline regions in the cAFM can also be observed with an optical microscope.

A conductivity several orders of magnitude smaller compared to the in-plane direction was also confirmed by conductive AFM measurements on both BTT COF films on gold substrates (Figure 4d). As shown in Figure 4c, a current of up to 0.97 nA is observed at the polycrystalline non-oriented COF deposits on the film, where charge transport along the covalent bonds in these areas is possible in all spatial directions (Figures 4f and 2b–e). The strong suppression of charge transport in the out-of-plane direction shown by our experimental measurements could be the result of structural defects along the molecular stacks. With only weak bonds between the layers in the columnar stacking and a hopping-based transport, these single deviations of the AA stacking can represent barriers that suppress the charge transport effectively.

Overall, the electrical conductivity measurements show strongly directional, defect-dominated charge transport in the BTT COF films and, given the more than five orders of magnitude transport anisotropy, with a strong preference for the in-plane direction within the conjugated 2D-planes over the out-of-plane direction. Both the strong channel length dependence and cAFM in-plane measurements on a microscopic scale suggest that the room temperature conductivities of $\approx 8.7 \times 10^{-4}$ for the BTT TTA and $\approx 1.1 \times 10^{-4}$ S m⁻¹ for the BTT TTTBA represent only a lower limit, since they were measured on a macroscopic scale and depend strongly on the charge traps in the measured channel.

2.5. Charge-Carrier-Pathway Simulations

The possible charge-carrier migration pathways in BTT TTTBA were studied using classical molecular-dynamics (MD) simulations and subsequent charge-propagation simulations. The thermal fluctuations of the structure were studied with classical MD using the Universal Force Field (UFF)^[27] with AM1^[28,29] atomic charges.

A snapshot from the end of the simulation (Figure 5a) was used for imaginary-time-evolution simulations^[30] of electron- and hole-transport. The charge-transport simulations for electrons and holes are based on the local electron affinity^[31] (Figure 5b) and the local average ionization energy^[32] (Figure 5c), calculated using AM1^[28,29] semiempirical molecular-orbital (MO) theory. The calculated conductance paths for electrons and holes are shown in Figure 5d,e and Figure S17 (Supporting Information), respectively. Details of the simulations are given in the Supporting Information.

Contrary to our initial expectations, the charge transport along the columns perpendicular to the COF-plane shows a continuous path, which would indicate that perfect COF-crystals conduct strongly in this direction (Figure 5e; Figure S17d, Supporting Information). The conduction paths in the COF-plane (Figure 5d; Figure S17a–c, Supporting Information) indicate facile hopping conduction via tunneling between the

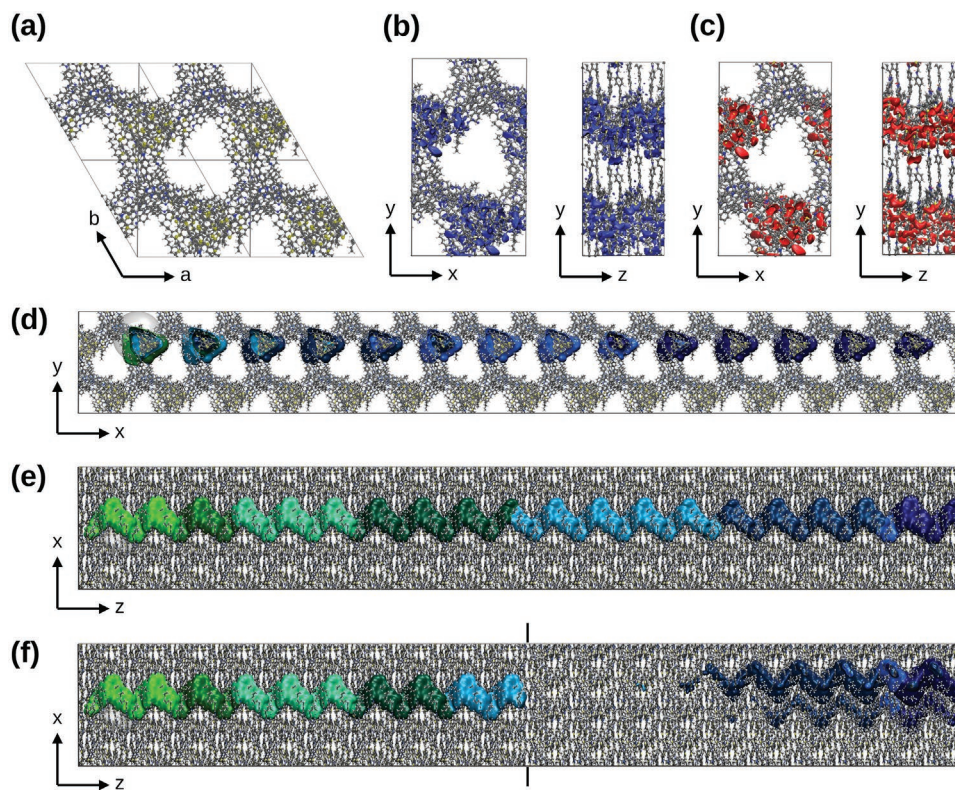


Figure 5. a) Top view of the equilibrated BTT TTTBA after 11 ns MD run. Top and side views of the isovalue-surfaces of the EA_L (blue, contour level = −1 eV) b) and IE_L (red, contour level = 14 eV) c) for BTT TTTBA calculated with AM1. The Cartesian directions (x, y, z) used for the charge-transport simulations relate to the crystallographic axes (a, b, c) in the following manner: x = a; y = 2b + a; z = c. Calculated electron-transport paths for the BTT TTTBA in the Cartesian directions x (d) and z (e). Isocontour plots for eight simulation steps of the electron (green to blue; contour level = 1.2 × 10⁻⁵ e-Bohr⁻³). The initial Gaussian functions are shown as transparent spheres. f) Calculated electron-transport path in the Cartesian z direction for the displaced model structure of the BTT TTTBA COF.

sulfur-rich centers. This conduction mechanism is consistent with the experimental results.

To estimate the effect of grain boundaries parallel to the plane of the COF between crystallites, a 180° rotation was introduced into the structure at the position of the dashed line in Figure 5f and Figure S17e (Supporting Information). The charge-transport simulations now show a significant barrier at this boundary (which is far tighter than expected in the real system). This barrier can only be crossed by tunneling. Figure 5f and Figure S17e (Supporting Information) show this behavior for an electron and a hole, respectively. The tunneling distance is clearly far larger than that in the in-plane paths between sulfur-rich centers.

3. Conclusions

In summary, we showed the synthesis of a novel three-pod thiophene-extended based tricarbaldehyde. In combination with different three-pod triazine-based amines we were able to synthesize two new highly crystalline, porous and imine-linked COF structures, namely BTT TTA and BTT TTTBA. To study their transport properties, the frameworks were successfully grown on different substrates using the in situ approach as electroactive, highly oriented thin films and room-temperature in-plane conductivities of up to 10^{-4} S m⁻¹ were measured. Temperature dependent electrical conductivity measurements revealed a temperature dependence indicative of trap-dominated hopping type charge transport. All in all, with our measurements we identified a strongly directional, defect-dominated charge transport in the BTT COF films, with a strong preference for the in-plane direction within the conjugated 2D planes over the out-of-plane direction. Quantum mechanical calculations predict a hopping type charge transport in the 2D molecular planes, and molecular COF columns perpendicular to the in-plane direction to provide a continuous path. By imposing a grain boundary in the form of a rotated COF layer, dramatically hampered charge transport in this direction. This study emphasizes the role of defect in the overall conductivity performance of COF materials and particularly for BTT COFs presented, where the electrical conductivity values obtained for the latter represent the lower limit and are expected to improve dramatically by defect-controlled synthesis strategies.

4. Experimental Section

General: All materials were purchased from Sigma–Aldrich, Acros or TCI Europe in the common purities "purum," "puriss," or "reagent grade." The materials were used as received without additional purification and handled in air unless otherwise noted.

BTT(T)₃ Building Block Synthesis: The BTT core was obtained following a reported protocol.^[3] Subsequently, the BTT core was stannylated and coupled to 5-bromo-4-butylthiophene-2-carbaldehyde through a *Stille* coupling reaction to afford the desired C₃-building block BTT(T)₃ (for more information see the Supporting Information).

BTT COF Thin Film Synthesis: The thin films were synthesized using a bottom-up, in situ approach. An autoclave equipped with a teflon liner and a substrate was charged with BTT(T)₃ (4.99 mg, 16.7 μmol) and TTA (2.37 mg, 10.0 μmol) or TTTBA (3.9 mg, 10 μmol). Next, a mixture of mesitylene and 1,4-dioxane (2000 μL, v:v 8:1) and 200 μL of acetic acid

(aqueous, 6 M) were added. The autoclave was sealed and heated at 120 °C for 16 h. After cooling to room temperature, the COF film was rinsed with anhydrous THF and dried under reduced pressure. The thickness of the resulting films could be increased by increasing the reaction time.

In-Plane Conductivity Measurements: The temperature-dependent transport measurements were performed at a Lakeshore CRX-VF probe station at vacuum conditions with $p < 2 \times 10^{-7}$ mbar. The electrical gold contacts (60 nm thickness) were evaporated through a shadow mask. An electrically conductive sample stage was used for gating through the back gate. This stage was thermally coupled to a helium refrigerator allowing for measurements from 6 K to room temperature. Two source meters (Keithley 2450) were used to apply source-drain and gate voltages.

Out-of-Plane Conductivity Measurements: The conductive AFM (cAFM) measurements were performed on a Jupiter XR AFM by Oxford Instruments using SCM-PIT conductive AFM tips with PtIr5 coating. The BTT COF films for this analysis were grown on glass substrates covered by a gold layer.

Charge-Carrier Pathway Simulations: A hexagonal simulation cell of dimensions 35.0 × 35.0 × 32.0 Å was constructed for BTT TTTBA by stacking eight unit cells. The UFF force field with AM1 Coulson charges was used for the classical molecular-dynamics (MD) simulations. The system was prepared using slightly modified tools developed by Boyd et al.^[33] A cutoff of 12.5 Å was used for the nonbonding interactions; Coulomb interactions beyond this distance were treated using a particle–particle Ewald approach.^[34] The system was equilibrated for 1 ns and an additional 10 ns simulation using a Nosé–Hoover thermostat and barostat in the anisotropic NPT ensemble (1 fs time step, 298 K, 1 atm, 100 timesteps temperature damping, 10 000 timesteps pressure damping), using LAMMPS.^[35] A snapshot taken at the end of the simulation was used for further processing.

Semiempirical molecular-orbital (MO) single-point calculations with periodic boundary conditions using the AM1 Hamiltonian within the restricted Hartree–Fock formalism were carried out using the cluster version of EMPIRE 20.^[36] The calculations were performed on the nearly hexagonal simulation cell of BTT TTTBA of dimensions 34.4 × 34.1 × 25.0 Å consisting of 1200 atoms. 3D local electron affinity and local-ionization energy maps were generated with EH5cube 20^[37] and stored in Gaussian cube-file format^[38] as orthogonal cells of 34.4 × 59.1 × 25.0 Å.

Propagation of the hole- or electron density in imaginary time used an in-house program.^[39] Simulations of electron and hole charge-transport in the different Cartesian directions were performed on supercells of the electron affinity and local-ionization energy maps by applying a linear term describing a homogeneous electric field in the appropriate direction to the external potential, as described in Ref. [39]. The results were visualized using Vpster v1.19.1b^[40] and VMD 1.9.1.^[41]

Supporting Information

Supporting Information is available from the Wiley Online Library or from the author.

Acknowledgements

The authors acknowledge Dr. Steffen Schmidt for the preparation of the SEM images. The authors thank Dr. Markus Döblinger for electron microscopy. The authors are grateful for financial support from the Excellence Clusters "Nanosystems Initiative Munich (NIM)", the Free State of Bavaria through the Research Network "Solar Technologies go Hybrid" and the Deutsche Forschungsgemeinschaft (DFG, German Research Foundation) in the COORNets SPP 1928 Projects WE 4893–6, ME 4515/1–2, and CL 85/24–2. RTW acknowledges partial funding from Germany's Excellence Strategy – "EXC 2089/1–390776260 (e-conversion)".

Open access funding enabled and organized by Projekt DEAL.

Conflict of Interest

The authors declare no conflict of interest.

Author Contributions

L.F. and J.F.P. contributed equally to this work. The manuscript was written through contributions of all authors. All authors have given approval to the final version of the manuscript.

Data Availability Statement

The data that support the findings of this study are available from the corresponding author upon reasonable request.

Keywords

benzotrithiophene, covalent organic frameworks, electrical conductivity, thin films

Received: May 25, 2022

Revised: July 21, 2022

Published online: August 24, 2022

- [1] a) L. Frey, J. J. Jarju, L. M. Salonen, D. D. Medina, *New J. Chem.* **2021**, 45, 14879; b) M. S. Lohse, T. Bein, *Adv. Funct. Mater.* **2018**, 28, 1705553.
- [2] a) H. Fan, A. Mundstock, A. Feldhoff, A. Knebel, J. Gu, H. Meng, J. Caro, *J. Am. Chem. Soc.* **2018**, 140, 10094; b) Z. Li, X. Feng, Y. Zou, Y. Zhang, H. Xia, X. Liu, Y. Mu, *Chem. Commun.* **2014**, 50, 13825.
- [3] a) L. Ascherl, E. W. Evans, J. Gorman, S. Orsborne, D. Bessinger, T. Bein, R. H. Friend, F. Auras, *J. Am. Chem. Soc.* **2019**, 141, 15693; b) S. Jhulki, A. M. Evans, X.-L. Hao, M. W. Cooper, C. H. Feriante, J. Leisen, H. Li, D. Lam, M. C. Hersam, S. Barlow, J.-L. Brédas, W. R. Dichtel, S. R. Marder, *J. Am. Chem. Soc.* **2020**, 142, 783; c) Y. Wang, Z. Zhao, G. Li, Y. Yan, C. Hao, *J. Mol. Model.* **2018**, 24, 153.
- [4] a) Y. Wang, H. Liu, Q. Pan, C. Wu, W. Hao, J. Xu, R. Chen, J. Liu, Z. Li, Y. Zhao, *J. Am. Chem. Soc.* **2020**, 142, 5958; b) J.-C. Shen, W.-L. Jiang, W.-D. Guo, Q.-Y. Qi, D.-L. Ma, X. Lou, M. Shen, B. Hu, H.-B. Yang, X. Zhao, *Chem. Commun.* **2020**, 56, 595.
- [5] a) W.-R. Cui, C.-R. Zhang, W. Jiang, F.-F. Li, R.-P. Liang, J. Liu, J.-D. Qiu, *Nat. Commun.* **2020**, 11, 436; b) N. A. Khan, R. Zhang, H. Wu, J. Shen, J. Yuan, C. Fan, L. Cao, M. A. Olson, Z. Jiang, *J. Am. Chem. Soc.* **2020**, 142, 13450.
- [6] D. D. Medina, M. L. Petrus, A. N. Jumabekov, J. T. Margraf, S. Weinberger, J. M. Rotter, T. Clark, T. Bein, *ACS Nano* **2017**, 11, 2706.
- [7] A. Fukazawa, H. Oshima, S. Shimizu, N. Kobayashi, S. Yamaguchi, *J. Am. Chem. Soc.* **2014**, 136, 8738.
- [8] W. Budiawan, K.-W. Lai, P. Karuppuswamy, T. S. Jadhav, Y.-A. Lu, K.-C. Ho, P.-C. Wang, C.-C. Chang, C.-W. Chu, *ACS Appl. Mater. Interfaces* **2020**, 12.
- [9] A. Molina-Ontoria, I. Zimmermann, I. Garcia-Benito, P. Gratia, C. Roldán-Carmona, S. Aghazada, M. Graetzel, M. K. Nazeeruddin, N. Martín, *Angew. Chem., Int. Ed.* **2016**, 55, 6270.
- [10] S. N. Afraj, C.-C. Lin, A. Velusamy, C.-H. Cho, H.-Y. Liu, J. Chen, G.-H. Lee, J.-C. Fu, J.-S. Ni, S.-H. Tung, S. Yau, C.-L. Liu, M.-C. Chen, A. Facchetti, *Adv. Funct. Mater.* **2022**, 32, 2200880.
- [11] a) W. Chen, G. Huang, X. Li, Y. Li, H. Wang, H. Jiang, Z. Zhao, D. Yu, E. Wang, R. Yang, *ACS Appl. Mater. Interfaces* **2019**, 11, 33173; b) Q. He, M. Shahid, J. Panidi, A. V. Marsh, W. Huang, M. Daboczi, J.-S. Kim, Z. Fei, T. D. Anthopoulos, M. Heeney, *J. Mater. Chem. C* **2019**, 7, 6622.
- [12] X. Guo, S. R. Puniredd, M. Baumgarten, W. Pisula, K. Müllen, *J. Am. Chem. Soc.* **2012**, 134, 8404.
- [13] S. Rossi, A. Bisello, R. Cardena, L. Orian, S. Santi, *Eur. J. Org. Chem.* **2017**, 2017, 5966.
- [14] C. Gu, N. Huang, Y. Chen, L. Qin, H. Xu, S. Zhang, F. Li, Y. Ma, D. Jiang, *Angew. Chem., Int. Ed.* **2015**, 54, 13594.
- [15] Q. Xiao, T. Sakurai, T. Fukino, K. Akaike, Y. Honsho, A. Saeki, S. Seki, K. Kato, M. Takata, T. Aida, *J. Am. Chem. Soc.* **2013**, 135, 18268.
- [16] a) H. Wei, J. Ning, X. Cao, X. Li, L. Hao, *J. Am. Chem. Soc.* **2018**, 140, 11618; b) Y. Song, L. Guo, Y. Du, L. Yang, L. Wang, *Chem. Commun.* **2020**; c) X. Pan, X. Qin, Q. Zhang, Y. Ge, H. Ke, G. Cheng, *Micropor. Mesopor. Mat.* **2020**, 296, 109990.
- [17] M. S. Lohse, J. M. Rotter, J. T. Margraf, V. Werner, M. Becker, S. Herbert, P. Knochel, T. Clark, T. Bein, D. D. Medina, *CrystEngComm* **2016**, 18, 4295.
- [18] T. Sick, J. M. Rotter, S. Reuter, S. Kandambeth, N. N. Bach, M. Döblinger, J. Merz, T. Clark, T. B. Marder, T. Bein, D. D. Medina, *J. Am. Chem. Soc.* **2019**, 141, 12570.
- [19] G. H. V. Bertrand, V. K. Michaelis, O. Ta-Chung, R. G. Griffin, D. Mircea, *Proc. Natl. Acad. Sci. USA* **2013**, 110, 4923.
- [20] A. Mähringer, D. D. Medina, *Nat. Chem.* **2020**, 12, 985.
- [21] M. Thommes, K. Kaneko, A. V. Neimark, J. P. Olivier, F. Rodriguez-Reinoso, J. Rouquerol, K. S. W. Sing, *Pure Appl. Chem.* **2015**, 87, 1051.
- [22] A. P. Côté, A. I. Benin, N. W. Ockwig, M. O’Keeffe, A. J. Matzger, O. M. Yaghi, *Science* **2005**, 310, 1166.
- [23] a) T. Sick, A. G. Hufnagel, J. Kampmann, I. Kondofersky, M. Calik, J. M. Rotter, A. Evans, M. Döblinger, S. Herbert, K. Peters, D. Böhm, P. Knochel, D. D. Medina, D. Fattakhova-Rohlfing, T. Bein, *J. Am. Chem. Soc.* **2018**, 140, 2085; b) D. D. Medina, V. Werner, F. Auras, R. Tautz, M. Dogru, J. Schuster, S. Linke, M. Döblinger, J. Feldmann, P. Knochel, T. Bein, *ACS Nano* **2014**, 8, 4042; c) D. D. Medina, T. Sick, T. Bein, *Adv. Energy Mater.* **2017**, 7, 1700387.
- [24] Z. Liu, M. Kobayashi, B. C. Paul, Z. Bao, Y. Nishi, *Phys. Rev. B* **2010**, 82, 35311.
- [25] I. Vladimirov, C. Chow, A.-J. Strudwick, W. Kowalsky, M. G. Schwab, D. Kälblein, R. T. Weitz, *Phys. Status Solidi A* **2015**, 212, 2059.
- [26] a) M. Souto, D. F. Perepichka, *J. Mater. Chem. C* **2021**, 9, 10668; b) Y. Zhu, S. Jiang, X. Jing, X. Feng, *Trends Chem.* **2022**, 4, 128.
- [27] A. K. Rappe, C. J. Casewit, K. S. Colwell, W. A. Goddard, W. M. Skiff, *J. Am. Chem. Soc.* **1992**, 114, 10024.
- [28] M. J. S. Dewar, E. G. Zoebisch, E. F. Healy, J. J. P. Stewart, *J. Am. Chem. Soc.* **1985**, 107, 3902.
- [29] M. J. S. Dewar, Y. C. Yuan, *Inorg. Chem.* **1990**, 29, 3881.
- [30] a) M. Kriebel, D. Sharapa, T. Clark, *J. Chem. Theory Comput.* **2017**, 13, 6308; b) M. Kriebel, M. Hennemann, F. R. Beierlein, D. D. Medina, T. Bein, T. Clark, *J. Chem. Inf. Model.* **2019**, 59, 5057.
- [31] a) B. Ehresmann, M. J. de Groot, A. Alex, T. Clark, *J. Chem. Inf. Comp. Sci.* **2004**, 44, 658; b) T. Clark, *J. Mol. Model.* **2010**, 16, 1231.
- [32] P. Sjöberg, J. S. Murray, T. Brinck, P. Politzer, *Can. J. Chem.* **1990**, 68, 1440.
- [33] a) P. G. Boyd, S. M. Moosavi, M. Witman, B. Smit, *J. Phys. Chem. Lett.* **2017**, 8, 357; b) LAMMPS Interface 0.2.2. https://github.com/peteboyd/lammps_interface.
- [34] T. Darden, D. York, L. Pedersen, *J. Chem. Phys.* **1993**, 98, 10089.
- [35] a) LAMMPS version 12, <http://lammps.sandia.gov>; b) S. Plimpton, *J. Comput. Phys.* **1995**, 117, 1.
- [36] a) EMPIRE 20, Cepos InSilico GmbH Obermichelbach, <http://ceposinsilico.de/products/empire.html>; b) M. Hennemann, T. Clark, *J. Mol. Model.* **2014**, 20, 2331; c) J. T. Margraf, M. Hennemann, T. Clark, *J. Mol. Model.* **2020**, 26, 43;

- d) J. T. Margraf, M. Hennemann, B. Meyer, T. Clark, *J. Mol. Model.* **2015**, 21, 144.
- [37] EH5cube 20, Cepos InSilico GmbH Obermichelbach, <http://ceposinsilico.de/products/empire.htm>.
- [38] can be found under <https://gaussian.com/cubegen/>.
- [39] M. Kriebel, D. Sharapa, T. Clark, *J. Chem. Theory Comput.* **2017**, 13, 6308.
- [40] S. Gsänger, Vipster 1.19.1 b, <https://sgsaenger.github.io/vipster/index.html>.
- [41] a) VMD1.9.1. <http://www.ks.uiuc.edu/Research/vmd/>; b) W. Humphrey, A. Dalke, K. Schulten, *J. Mol. Graphics* **1996**, 14, 33.